ARTICLES

Journal of Semiconductors
(2023) 44, 072806
doi: 10.1088/1674-4926/44/7/072806

Surface plasmon assisted high-performance photodetectors based on hybrid TiO_2@GaO_xN_y-Ag heterostructure

Jiajia Tao[1, ‡], Guang Zeng[1, ‡], Xiaoxi Li[1], Yang Gu[1], Wenjun Liu[1, †], David Wei Zhang[1, 2], and Hongliang Lu[1, 2, †]

[1]State Key Laboratory of ASIC and System, Shanghai Institute of Intelligent Electronics & Systems, School of Microelectronics, Fudan University, Shanghai 200433 , China

[2]Jiashan Fudan Institute, Jiaxing 314100, China

Abstract: In this work, we reported a high-performance-based ultraviolet-visible (UV-VIS) photodetector based on a TiO_2@GaO_xN_y-Ag heterostructure. Ag particles were introduced into TiO_2@GaO_xN_y to enhance the visible light detection performance of the heterojunction device. At 380 nm, the responsivity and detectivity of TiO_2@GaO_xN_y-Ag were 0.94 A/W and 4.79×10^9 Jones, respectively, and they increased to 2.86 A/W and 7.96×10^{10} Jones at 580 nm. The rise and fall times of the response were 0.19/0.23 and 0.50/0.57 s, respectively. Uniquely, at 580 nm, the responsivity of fabricated devices is one to four orders of magnitude higher than that of the photodetectors based on TiO_2, Ga_2O_3, and other heterojunctions. The excellent optoelectronic characteristics of the TiO_2@GaO_xN_y-Ag heterojunction device could be mainly attributed to the synergistic effect of the type-Ⅱ band structure of the metal–semiconductor–metal heterojunction and the plasmon resonance effect of Ag, which not only effectively promotes the separation of photogenerated carriers but also reduces the recombination rate. It is further illuminated by finite difference time domain method (FDTD) simulation and photoelectric measurements. The TiO_2@GaO_xN_y-Ag arrays with high-efficiency detection are suitable candidates for applications in energy-saving communication, imaging, and sensing networks.

Key words: TiO_2@GaO_xN_y-Ag; ultraviolet-visible; photodetector; type-Ⅱ band structure; plasmon resonance effect

Citation: J J Tao, G Zeng, X X Li, Y Gu, W J Liu, W Zhang, and H L Lu, Surface plasmon assisted high-performance photodetectors based on hybrid TiO_2@GaO_xN_y-Ag heterostructure[J]. *J. Semicond.*, 2023, 44(7), 072806. https://doi.org/10.1088/1674-4926/44/7/072806

1. Introduction

Ultraviolet optoelectronics is a key technology of future information development. Recently, as a critical ultraviolet optoelectronic device, high-performance ultraviolet photodetectors have received considerable attention and have been applied in high-voltage power transmission, fire detection, and ozone hole detection. Therefore, different wide bandgap semiconductor materials, such as AlGaN, MgZnO, Ga_2O_3, SnO_2, TiO_2, have been utilized for the development of high-performance UV detectors, which have considerably improved device performance in the past ten years[1–5]. In particular, TiO_2 is one of the most practical optoelectronic materials that have been widely used in catalytic reactions and optoelectronic devices. The bandgap of TiO_2 is 3.2 eV, thus it determines its light absorption only in the ultraviolet region[6]. Moreover, the one-dimensional TiO_2 nanowire array exhibits the unique advantage of high aspect ratio, which brings its efficient electron transport and excellent stability. The performance of one-dimensional TiO_2 nanowire array photodetectors is superior to that of the conventional TiO_2 film, which is ascribed to the nanowire structure that increases the reflection and absorption of light trapping and increases the adsorption area of oxygen on TiO_2[7]. However, it also should be mentioned that the internal intrinsic defects and optical characteristics in a specific wavelength range of the nanowire structure deteriorate the development as photodetectors. In order to further improve the performance of TiO_2 nanowire array photodetectors, sophisticated techniques such as doping, hydrogenation reduction/defect engineering, loading nanoparticles of plasma metal, semiconductor nanocrystals (or quantum dots), and molecular dye sensitisation have been implemented[8, 9]. It demonstrates the above methods can not only improve the quality and material system of TiO_2 but also widen its optical absorption band edge to the visible or even the near-infrared region[10]. Consequently, the one-dimensional ordered TiO_2 core–shell structure has become the most effective strategy for improving photodetection performance because of its large heterogeneous interface area, short diffusion length, direct carrier transport channel, and high specific surface area[11, 12].

Anion engineering provides a strategy for transformation of the electronic energy band structure. Considering the role of N introduced in the oxynitriding process, it is reported that the repulsive force caused by the hybrid metal three-dimensional orbital of N 2*p*, O 2*p*, and *p*-*d* increases the valence band to the maximum, which can not only suppress the continuous photoconductivity effect but also reduce the oxide bandgap and improve the optical performance[12]. In the earlier days, amorphous nitrogen-doped oxides and oxyni-

Jiajia Tao and Guang Zeng contributed equally to this work and should be considered as co-first authors.

Correspondence to: W J Liu, wjliu@fudan.edu.cn; H L Lu, hongliang lu@fudan.edu.cn

Received 28 DECEMBER 2022; Revised 16 MARCH 2023.

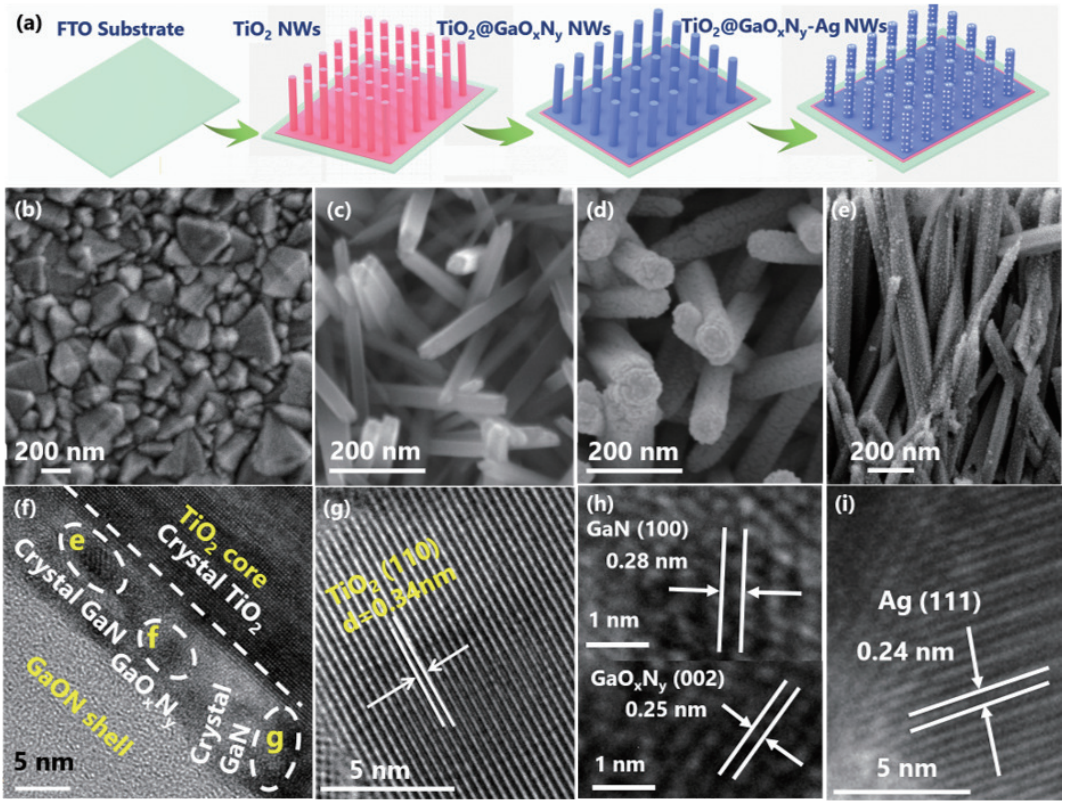

Fig. 1. (Color online) (a) TiO_2@GaO_xN_y-Ag heterojunction preparation process. SEM image of (b) FTO, (c) TiO_2, (d) TiO_2@GaO_xN_y and (e) TiO_2@GaO_xN_y-Ag. (f) The TEM image of TiO_2@GaO_xN_y-Ag. (g) corresponds to the HRTEM image of TiO_2 in Fig. 1(f). (h) corresponds to the GaN and GaO_xN_y in the 'e', 'f', and 'g' regions in Fig. 1(f). (i) corresponds to the HRTEM image of the Ag nanoparticle.

trides have been studied in the field of thin-film transistors and energy storage[13, 14], however only a few studies have focused on photodetectors. Lately, literature reported that device fabricated by GaO_xN_y exhibits a low dark current, which realizes the improvement of device spectral sensitivity and the response time. At this moment, it is inferred that the construction of a core-shell structure heterojunction nanowire array based on TiO_2 and GaO_xN_y may help in developing high-performance photodetectors. Currently, the preparation of one-dimensional ordered core-shell nanostructures is mainly concentrated on chemical methods, sputtering, chemical vapour deposition, and other physical and chemical methods. Compared to these methods, the atomic layer deposition (ALD) technology can achieve low temperature, precise controllability, and unique nanostructures with large area uniformity[15]. Based on nano-core-shell arrays, many promising applications, such as transistor arrays, sensor arrays, transparent electrodes, and energy harvesters, have been developed[16, 17]. Therefore, high-throughput, low-cost, and large-scale preparation of one-dimensional, level-ordered, core–shell nanostructures, and high-performance photodetectors can be realised using TiO_2 nanowire arrays and plasma-enhanced atomic layer deposition (PE-ALD) to prepare GaO_xN_y.

Surface plasmon resonance (SPR) originates from the interaction of visible light and free electrons of nanometals, and it can effectively produce high-energy carriers or hot electrons under the illumination of light[18]. However, physical evidences indicate that the SPR or localized SPR (LSPR) will be attenuated rapidly by the scattering of vibrational electrons in the conduction band or generation of hot carriers in the metal within a femtosecond[19]. Therefore, arresting the carriers that generated by SPR before decay, and converting them will be a huge advantage. Recently, the plasma metal–semiconductor junction produces superior spectral sensitivity and light responsivity in a specific spectral range, when it compares with the usual diode comprised by the semiconductor that the inter-band transition dominated in the photocurrent generation[20]. The plasma element functions as a visible-light-sensitive layer can generate numerous carriers, whereas the semiconductor material functions as a carrier acceptor and provides an effective transmission path[21]; this synergistic system can be used for the development of novel, next-generation visible light photodetectors. Metal–semiconductor (MS) junctions composed of precious metals, such as Au, Ag, and Cu, and semiconductors have been used as photodetectors[22]. Among these precious metals, Ag is favoured due to its excellent stability and low price. The application of Ag-nanoparticle heterojunctions and quantum-dot-modified semiconductors for photoelectric detection and energy has become a critical topic[23].

In this work, TiO_2 nanowire arrays, GaO_xN_y, and Ag nanoparticles and hydrothermal, PE-ALD, and photolysis methods were utilized to prepare a TiO_2@GaO_xN_y-Ag heterogeneous material through a three-step method. Based on the heterojunction nanowire array of the ternary system, a metal–semiconductor–metal (MSM) photodetector was constructed, and its performance and internal mechanism were tested and analysed in detail.

2. Results and discussion

Fig. 1(a) shows the flowchart of preparing the

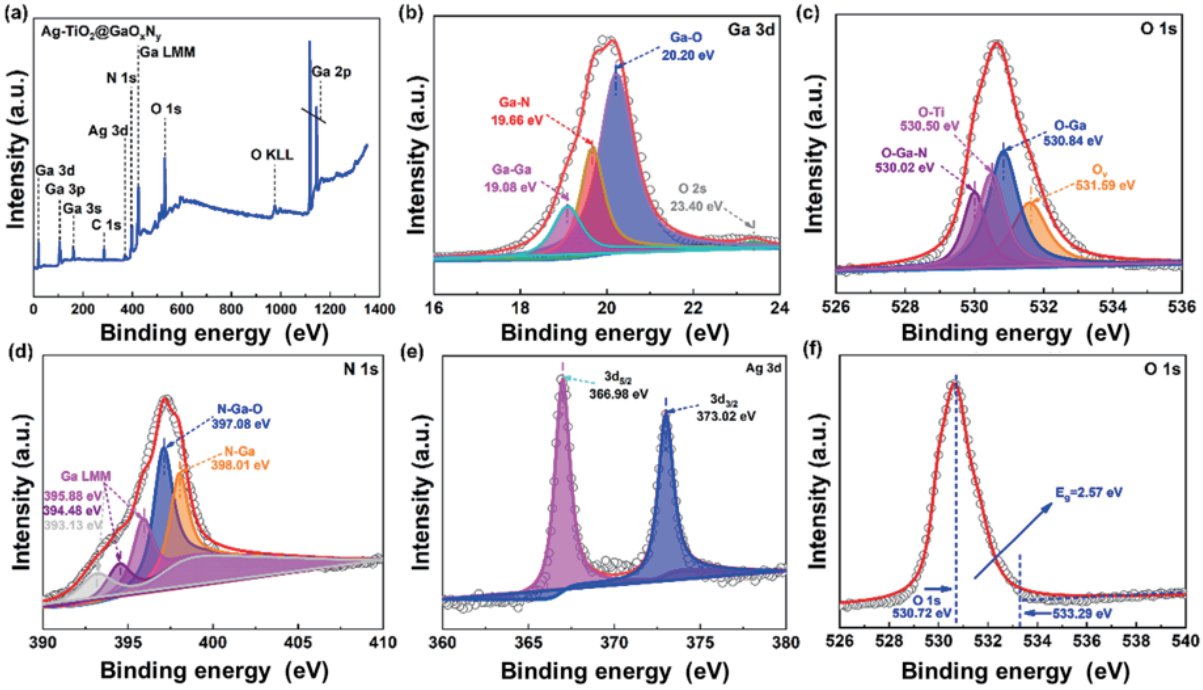

Fig. 2. (Color online) (a) XPS survey spectrum. High-resolution spectra of (b) Ga 3*d*, (c) O 1*s*, (d) N 1*s* and (e) Ag 3*d*. (f) The O 1*s* peak and inelastic scattering loss for TiO_2@GaO_xN_y-Ag heterojunction.

TiO_2@GaO_xN_y-Ag heterojunction. First, TiO_2 nanowire arrays were deposited on the fluorine-doped tin oxide (FTO) substrate by using the hydrothermal method. Then, the process parameters of ALD were varied to control the growth of the GaO_xN_y film on the TiO_2 nanowire array to form a TiO_2@GaO_xN_y core–shell heterojunction nanowire array. Finally, photolysis was used to synthesize the Ag nanoparticles on the heterojunction array to form a TiO_2@GaO_xN_y-Ag ternary heterojunction nanowire array[24]. Fig. 1(b) displays the scanning electron microscope (SEM) image of FTO and it is observed that FTO morphology primarily comprises nanoparticles with various sizes. The lattice of FTO and rutile TiO_2 (TiO_2: $a = b = 0.4517$ nm, FTO: $a = b = 0.4687$ nm) matched very well[25]. These FTO particles are the basis for the deposition of TiO_2 nanowires. Fig. 1(c) illustrates the TiO_2 nanowire array grown after the hydrothermal reaction. The nanowires were regular and uniform, the sidewalls were smooth. The tips of the nanowires were protruding, with the diameter and length of ~140 nm and 4.5 nm, respectively. These regular large-surface-area TiO_2 nanowire arrays are conducive for the effective PE-ALD deposition of GaO_xN_y. The process of preparing GaO_xN_y film by PE-ALD is shown in Ref.[26]. The morphology of the TiO_2 nanoarray after PE-ALD deposition is shown in Fig. 1(d). GaON was uniformly coated on the surface of the TiO_2 nanowire array, and the shell of GaON was approximately 10 nm, and a unique TiO_2@GaO_xN_y core-shell heterojunction nanowire array was formed. The heterojunction array was placed in a 0.1 M $AgNO_3$ solution, and the morphology of the sample was obtained by photodecomposition under ultraviolet light to modify the Ag particles. Fig. 1(e) depicts that Ag nanoparticles were uniformly distributed on the sidewall and the top of the TiO_2@GaO_xN_y core-shell structure heterojunction nanowire array, forming a uniform ternary TiO_2@GaO_xN_y-Ag heterojunction array. Meanwhile, the statistical distribution of the Ag nanoparticle size was also investigated. As displayed in Fig. S1, most Ag particles were 20 nm in size, showing the uniformity of prepared Ag particles.

Fig. 1(f) depicts the transmission electron microscopy (TEM) scan-performed on the TiO_2@GaO_xN_y-Ag. The GaO_xN_y layer was composed of GaN and GaON crystalline parts and amorphous components. The interplanar spacing of 0.34 nm corresponds to the (110) crystal plane of rutile TiO_2, evidenced by high-resolution TEM (HRTEM), which in Fig. 1(g) revealed that the prepared TiO_2 has a crystal nature. The further analysis of areas 'e', 'f', and 'g' are shown in Fig. 1(h). The interplanar spacing of 0.28 nm corresponds to the (100) crystal plane of GaN, which is consistent with the reported result[27]. As shown in Fig. 1(h), the interplanar spacing of 0.25 nm corresponded to the GaO_xN_y (002) crystal plane, agreeing well with the results[28]. Based on the aforementioned results, it revealed that GaO_xN_y contained not only GaN and GaO_xN_y crystals but also amorphous Ga_2O_3 or GaN and GaON[29, 30]. Besides, the results of spectroscopic ellipsometry (SE) characterization for 200-cycles GaO_xN_y layers deposited by PE-ALD were shown in Fig. S2**,** which were consistent with the growth rate and physical characteristics of GaO_xN_y film. The interplanar spacing of 0.24 nm in Fig. 1(i) corresponded to Ag (111) crystal planes, in line with X-ray diffractometer (XRD) results in Fig. S3. The presence of Ag in the junction was mainly in the form of elemental Ag nanoparticles. The above analysis suggested that the successful preparation of a ternary TiO_2@GaO_xN_y-Ag heterojunction nanowire structure with uniform morphology, controllable rules, purity, and high quality.

The survey X-ray photoelectron spectroscopy (XPS) spectrum in Fig. 2(a) of the TiO_2@GaO_xN_y-Ag heterojunction revealed that it contained only Ga, O, Ag, N, and C elements. No Ti element was observed because the effective detection depth of XPS was 0–10 nm. The thickness of Ag and GaO_xN_y

on the TiO_2 surface was greater than 10 nm, as shown in Fig. 1(e). The XPS results of TiO_2 were also shown in Fig. S4, proving the pure TO_2 nanowires. Ar was engraved for 10 s to determine the internal elements and valence states of the sample. Fig. 2(b) depicts a high-resolution XPS image of Ga element after Ar engraving. The main peak of Ga 3*d* was divided into four peaks of 19.08, 19.66, 20.20, and 23.40 eV, which corresponded to the Ga-Ga, Ga-N, Ga-O bonds, and O 2*s* peak positions, respectively. The area of the Ga-N bond was larger than that of the Ga-O bond even under the condition that the flow ratio of NH_3:O_2 was 95:5 sccm. This revealed that the activity of the O_2 plasma was higher than that of the NH_3 plasma. The Ga-N and Ga-O bonds suggested that both O_2 and NH_3 can react with Ga-CH_3 simultaneously and compete with each other, implying the presence of a GaN/Ga_2O_3 heterojunction, and the Ga_2O_3 content was more than that of GaN. As presented in Fig. 2(c), the main peak of O 1*s* was divided into four peaks at 530.02, 530.50, 530.84, and 531.59 eV, corresponding to the O-Ga-N, O-Ti, and O-Ga bonds, and O_v. The O_v peak is derived from oxygen defects and vacancies inside the film[31]. The bond energy of O-Ga-N is higher than that of Ga-O and N-Ga, indicating that the formation of the chemical bond is not a superposition of a single Ga_2O_3 and GaN. O-Ga-N resulted from the oxidation of the GaN surface and finally formed a single ternary nitrogen oxide of GaO_xN_y. The Ti-O bond originates from TiO_2 at the heterojunction interface. The Ga-O bond is due to the combination of Ga-O in Ga_2O_3, and the position of Ga-O is consistent with the other result[32].

Moreover, we performed peak separation on the main peak of N 1*s* to examine composition and the valence state of N in the heterojunction (Fig. 2(d)). In addition to the Ga LMM peaks of 395.88, 394.48, and 393.13 eV, N-Ga-O and N-Ga bonds of 397.08 eV and 398.01 eV were obtained[33]. The existence of N-Ga-O is in accordance with O-Ga-N bonds in the previous O 1*s* analysis, which indicated the presence of GaON. A multielement compound reveals that O atoms can replace the N atoms in the Ga-N bond during the ALD growth process. Furthermore, N can replace O in the Ga-O bond. By adjusting the flow rate and reaction temperature of NH_3 and N_2 during the ALD process, Ga_2O_3 and GaN can be doped to form n-type GaN or p-type Ga_2O_3. The results show the coexistence of Ga_2O_3, GaN, and GaO_xN_y in the heterojunction. The N and O content and the presence of multicomponent phases are conducive for the high performance of the photodetector[34]. The XPS spectrum of Ag 3*d* is displayed in Fig. 2(e). The main peaks were categorised into Ag $3d_{5/2}$ and Ag $3d_{3/2}$. The corresponding positions were 366.98 and 373.02 eV, and the distance between the two peaks was 6.04 eV[35]. It is evidenced that Ag was present mainly in the form of Ag^0[36, 37], indicative of a metallic Ag nanoparticle in a ternary system TiO_2@GaO_xN_y-Ag heterojunction. It consisted of pure TiO_2, multicomponent Ga_2O_3/GaN and GaO_xN_y, and elemental Ag particles. Furthermore, the determination of the E_g value of the TiO_2@GaO_xN_y-Ag heterojunction using the energy-loss peak of the O 1*s* spectrum was shown in Fig. 2(f). The obtained E_g value of TiO_2@GaO_xN_y-Ag heterojunction is 2.57 eV, which is smaller than that of TiO_2.

Next, we examined the photodetective performance of TiO_2@GaO_xN_y-Ag heterojunction by using the ultraviolet to visible light as the stimulating source. The photodetector based on a single TiO_2 and TiO_2@GaO_xN_y was also characterised. Fig. 3(a) shows the three-dimensional schematic diagram of the fabricated MSM photodetector with TiO_2@GaO_xN_y-Ag heterojunction. Fig. 3(b) depicts the corresponding optical image of the TiO_2@GaO_xN_y-Ag based photodetector. The length and width of the interfinger electrode are 20 and 1150 μm, respectively. The corresponding effective illumination area is 230 μm^2. Fig. 3(c) displays the photocurrent characteristics of the three devices at various wavelengths, with the fixed bias of 1 V, and optical power of 5.0 mW/cm^2. For the single TiO_2 device, the photocurrent decreases with the increase of the wavelength. And the maximum photocurrent was 3.0 A when the incident light wavelength was 380 nm, which is consistent with its intrinsic optical characteristics. However, for TiO_2@GaO_xN_y devices, the photocurrent gradually increased with an increase in wavelength, showing that the TiO_2@GaO_xN_y heterojunction formed by the introduction of the GaO_xN_y shell layer can effectively promote the absorption of visible light and the photogenerated current. Moreover, the photodetector of the TiO_2@GaO_xN_y-Ag heterojunction exhibited a maximum photocurrent of up to 65.1 A at the longest wavelength of 580 nm, which revealed that the introduction of Ag particles further strengthened the absorption and conversion efficiency of visible light and consequently improved photoelectricity. To further evaluate the performance of the photodetector of the TiO_2@GaO_xN_y-Ag heterojunction, the test was conducted in the dark at wavelengths of 380, 480, and 580 nm with the optical power of 5.0 mW/cm^2. The bias voltage was from −1 to 1 V. Fig. 3(d) shows that an extremely low dark current of 10^{-7} A was recorded under dark condition, which means fewer defects in the heterojunction. Thereafter, the photocurrent increased with an increase in the test wavelength. The photocurrent of the photodetector at 580 nm was 10^{-4} A, which was 10^3 times higher than the dark current. It shows the device can achieve excellent detectivity in the visible light region. Then, the light responsivity (*R*) and detection rate (*D*) were calculated according to the formula[38]. At 380 nm, the *R* and *D* of TiO_2@GaO_xN_y-Ag were 0.94 A/W and 4.79×10^9 Jones, respectively, whereas those at 580 nm were 2.86 A/W and 7.96×10^{10} Jones, respectively, which were considerably higher than those of the same type of photodetectors based on TiO_2, Ga_2O_3, and other heterojunction photodetectors listed in Table 1.

Next, we alternated between light and darkness every 30 s to determine the stability of the photodetector. The results of the light and dark test are presented in Fig. 3(e). The photocurrent increased and decayed rapidly with the presence or absence of light. The TiO_2@GaO_xN_y-Ag photodetector exhibited excellent stability and switching characteristics at wavelengths of 380, 480, and 580 nm. In addition to that, we also measured the characteristics of a single cycle of the device at various wavelengths, as illustrated in Figs. 3(f)–3(h). The rise time corresponds to the time when the current rises to 63% (1-1/e) of the maximum value, whereas the fall time corresponds to the current decreases to 37% of the maximum value (1/e) of the corresponding current. We evaluated the corresponding rise/fall times at 380, 480, and 580 nm as 0.19/0.23, 0.21/0.48, and 0.50/0.57 s, respectively. We can see from Fig. 3(i) that the TiO_2@GaO_xN_y-Ag photodetector

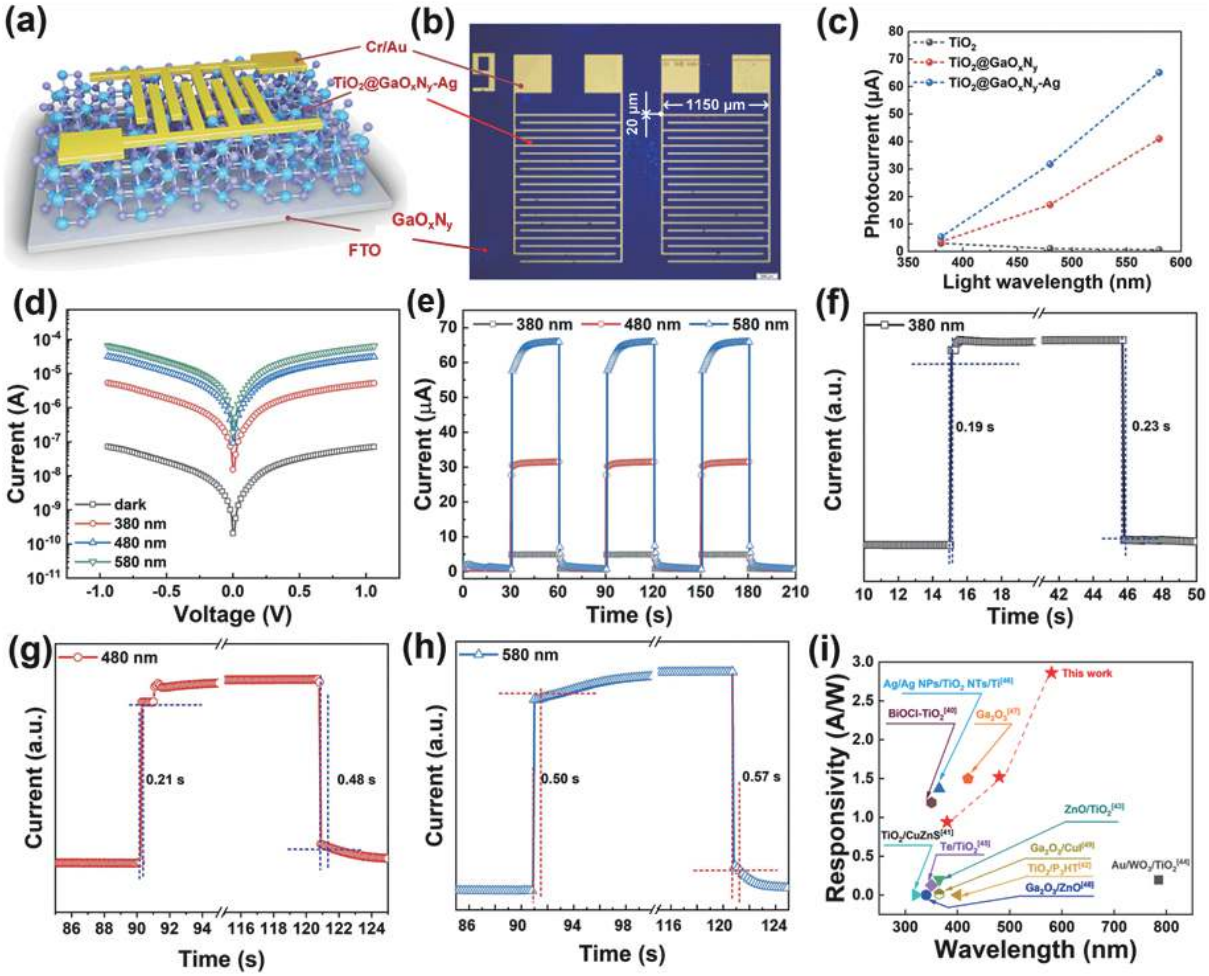

Fig. 3. (Color online) (a) The schematic of the structure of the TiO_2@GaO_xN_y-Ag photodetector. (b) The optical image of the fabricated photodetector. (c) Photocurrent change relationship of TiO_2, TiO_2@GaO_xN_y, and TiO_2@GaO_xN_y-Ag devices at various wavelengths; the bias voltage is 1 V, the optical power density is 5.0 mW/cm^2. (d) TiO_2@GaO_xN_y-Ag photocurrent change graph at 380, 480, and 580 nm wavelengths, bias voltage of -1 V to 1 V, optical power density of 5.0 mW/cm^2. (e) The current-time relationship diagram of the switch state under the aforementioned test conditions. (f) –(h) Light response time test diagrams at various wavelengths under the aforementioned test conditions. (i) Comparison of TiO_2@GaO_xN_y-Ag photodetector's performance in comparison to the reported TiO_2 and Ga_2O_3 heterojunction-based photodetector in the literature.

Table 1. Performance comparison of photodetectors based on TiO_2 and Ga_2O_3 heterojunctions.

Device structure	Light source (nm)	Bias (V)	D^* (Jones)	R_λ (A/W)	τ_r/τ_d (s)	Refs
Ga_2O_3/ZnO	340	10	–	1.5×10^{-4}	8.99/4.68	39
BiOCl-TiO_2	350	5	2.70×10^{13}	1.19	22.3/0.85	40
TiO_2/CuZnS	320	0	–	0.0021	0.2/0.2	41
TiO_2/P3HT	400	0	1.61×10^{10}	0.00031	1.1/0.5	42
ZnO/TiO_2	365	1	6.10×10^{9}	0.2	33.7/12	37
Au/WO_3/TiO_2	785	1	–	0.095	5.5×10^{-5}/1.1×10^{-4}	43
Te/TiO_2	350	0.5	–	0.125	–	44
Ag/Ag NPs/TiO_2 NTs/Ti	365	1	5.18×10^{10}	1.37	0.43/0.47	45
Ga_2O_3	420	4	–	1.5	0.4/0.46	46
TiO_2@GaO_xN_y–Ag	380	1	4.79×10^{9}	0.94	0.19/0.23	This work
TiO_2@GaO_xN_y–Ag	480	1	5.25×10^{9}	1.52	0.21/0.48	This work
TiO_2@GaO_xN_y–Ag	580	1	7.96×10^{10}	2.86	0.50/0.57	This work

exhibits excellent performances from ultraviolet (380 nm) to visible (580 nm) wavelengths than that of other TiO_2- and Ga_2O_3-based heterojunctions.

Fig. 4(a) shows the absorption spectra of TiO_2, TiO_2@GaO_xN_y, and TiO_2@GaO_xN_y-Ag heterojunctions. It exhibits the optical absorption edge of TiO_2 was 366 nm, indicating that TiO_2 is sensitive to ultraviolet light. The optical absorption region was mainly concentrated in the ultraviolet region, and the utilisation rate of other bands was low. According to our previous work[47], the bandgap of the GaO_xN_y is ~3.46 eV. After GaO_xN_y modification, the absorption edge of the TiO_2@GaO_xN_y core-shell heterojunction was redshifted to

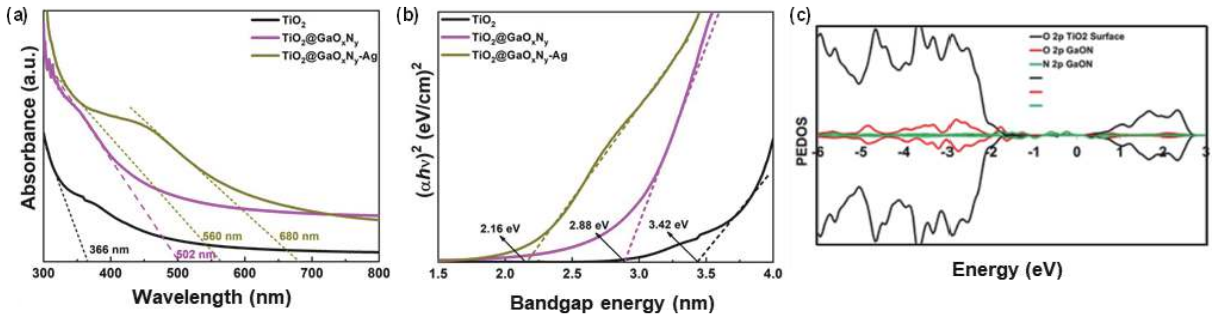

Fig. 4. (Color online) (a) UV-Vis absorption spectrum. (b) The relationship between $(ahv)^2$ and (hv). (c) Projected electronic density of states for the TiO_2@GaO_xN_y structure with the Fermi energy set to 0 eV.

502 nm because the GaO_xN_y shell enhanced the absorption of visible light bands and thus improved the optical properties. When the heterojunction was modified with Ag nanoparticles to form the ternary TiO_2@GaO_xN_y-Ag core-shell heterojunction, two absorption edges appeared at 560 and 680 nm because of the SPR effect of Ag particles. This effect enhanced the utilisation of visible light, improved the photoelectric conversion efficiency, and was highly conducive to the realisation of an efficient and fast photoelectric response. As shown in Fig. 4(b), according to the relationship between $(ahv)^2$ and (hv), the bandgap widths of TiO_2, TiO_2@GaO_xN_y, and heterojunction were 3.42, 2.88, and 2.16 eV, respectively, and the corresponding wavelengths were 362, 430 and 570 nm, respectively. Here, 570 nm also indicated that the presence of GaO_xN_y and Ag enhanced the absorption efficiency of TiO_2 to visible light.

The schematic of the electron band structure of Ga_2O_3 and GaO_xN_y is shown in Ref. [48]. Nitrogen replaced oxygen and thus reduced the density of trap states. In particular, the neutral oxygen defect near the top of the valence band was weakened or eliminated because of the hybridisation effect of the N 2*p* and O 2*p* orbitals. Alloying with nitrogen generated additional composite centres, which resulted in the recombination enhancement of nonequilibrium carriers of GaO_xN_y, thus possessing fast rise and fall times[48]. Fig. 4(c) shows the projected electron density of states (PEDOS) plots for the GaO_xN_y modified (110) crystal plane of rutile TiO_2 model system. It can be seen that a new energy band gap emerged by introducing GaO_xN_y clusters. A red shift in light absorption to a longer wavelength is identical with the experimental results, which confirms that the TiO_2@GaO_xN_y interfacial system enhancing visible light absorption. It is also found that stoichiometric ratio of GaO_xN_y has no obvious effect on the light absorption properties of TiO_2@GaO_xN_y.

Finally, FDTD simulation is performed to explain why Ag particles can realize the extraordinary absorption of TiO_2@GaOxNy-Ag heterostructure at a specific wavelength and broaden the detection wavelength range. The LSPR effect of the TiO_2@GaO_xN_y-Ag heterostructure was excited as Ag particles were present, which in turn achieves higher absorption at a specific wavelength. Fig. 5(a) shows the FDTD simulation model used for the extinction power calculation and local electric field distribution of the TiO_2@GaO_xN_y-Ag heterojunction at different wavelengths. In this simulation model, the Ag particles are defined as cubes with an edge length of 20 nm, and the thicknesses of the FTO, TiO_2, and GaO_xN_y are 5, 200, and 15 nm, respectively. Notably, the TiO_2 is completely covered by GaO_xN_y, which is located between the FTO substrate and the GaO_xN_y film. Boundary conditions for perfectly matched layers (PML) and a total field scattered field (TFSF) light source were used for the simulations. A detailed description of the simulation model can be found in the Simulation section of the supplementary information. Fig. 5(b) shows the calculated extinction power of pure TiO_2, TiO_2@GaO_xN_y, and TiO_2@GaO_xN_y-Ag at different wavelengths. Obviously, the TiO_2@GaO_xN_y structure has a higher absorption of incident light than the pure TiO_2 device on the FTO substrate, while the TiO_2@GaO_xN_y-Ag structure has a greater improvement in the absorption of incident light. It should be noted that with the increase of the wavelength of the incident light, the absorption of the incident light by this structure increases gradually and then decreases. But in a fairly wide wavelength range, the TiO_2@GaO_xN_y-Ag heterojunction photodetector has a high absorption of incident light. It shows that LSPR can broaden the material bandgap limit and thus make the detection range of the photodetector larger. Regarding the excitation of the LSPR effect by the Ag particles, it can be seen from the strong electric field distributions at the corresponding wavelengths in Figs. 5(c)–5(e). Further, for the incident light at 380, 480, and 580 nm, the electric field distribution gradually becomes stronger, which indicates that the TiO_2@GaO_xN_y-Ag heterojunction photodetector gradually enhances the absorption of incident light at these wavelengths. Generally speaking, the simulated absorption spectrum is in good agreement with the experimental results in terms of peak position, intensity, and shift. However, compared with the experimental results, the simulation results corresponding to Fig. 5(a) have large differences for the absorption intensities of GaO_xN_y device and TiO_2@GaO_xN_y-Ag heterojunctions. This may be due to the difference between the simulation model and the real sample, for example, the size of the Ag particles of the real sample is not all 20 nm. On the other hand, since the complex refractive index of the material is derived from previous papers or experimental results, the difference of these measurement conditions may lead to slight changes in the simulation results.

As shown in Fig. 6, the scheme and related energy band diagram are proposed to demonstrate the optoelectrical transport mechanism of the photodetector based on the TiO_2@GaO_xN_y-Ag heterojunction. As depicted in Fig. 6(a), under the UV-VIS illumination, the generated electron-hole pair of TiO_2@GaO_xN_y could provide more electrons and holes, which benefited for the electrical conductivity of the photodetector. Besides, the SPR effect of Ag nanoparticles decayed

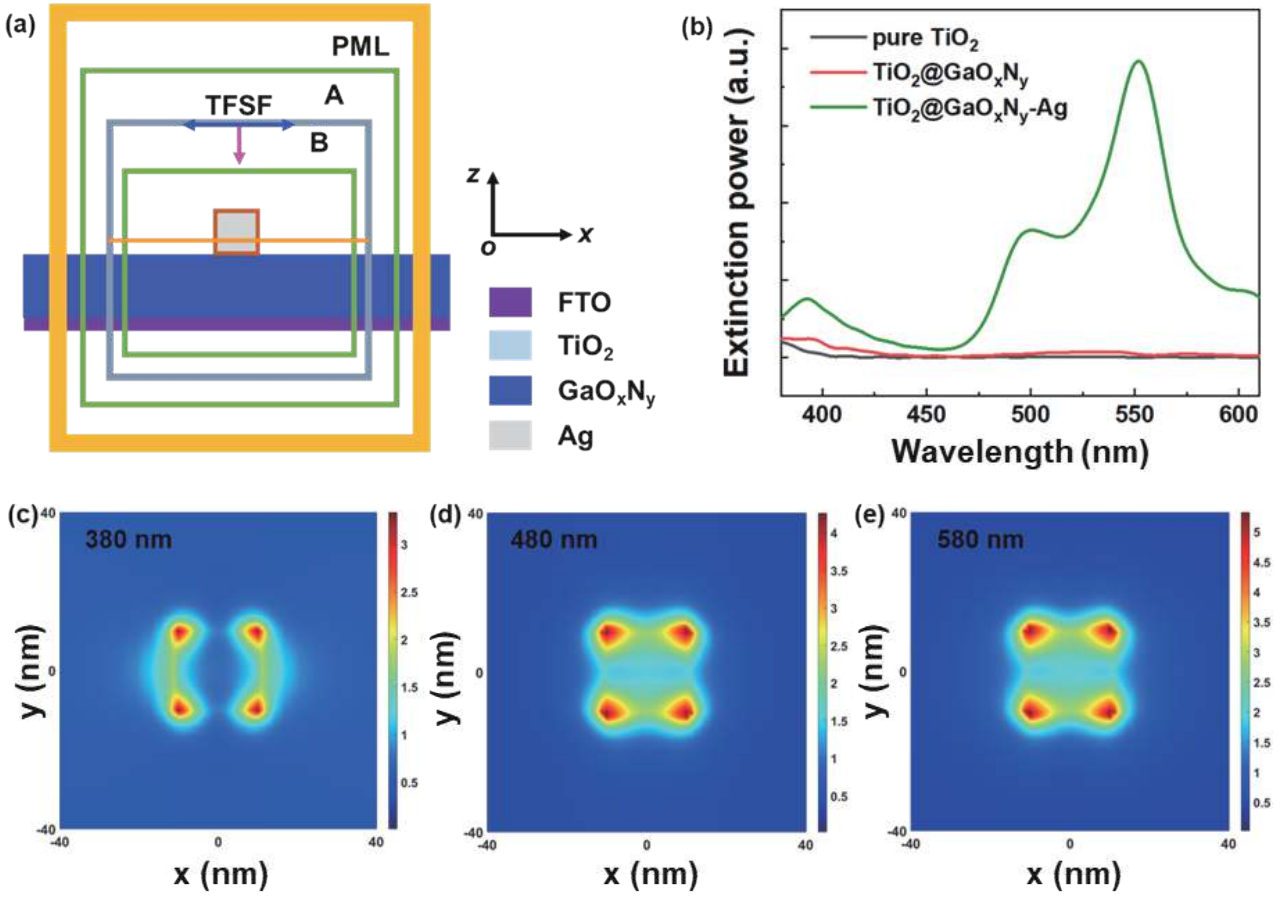

Fig. 5. (Color online) (a) Schematic illustration of the FDTD simulation setup used for the extinction power calculation and local electric field distribution of the TiO_2@GaO_xN_y-Ag heterojunction. (b) Calculated extinction power for the pure TiO_2, TiO_2@GaO_xN_y, and TiO_2@GaO_xN_y-Ag. The electric field distributions corresponding to the FDTD simulation of the TiO_2@GaO_xN_y-Ag heterojunction under different wavelengths of illumination (c) 380 nm; (d) 480 nm; (e) 580 nm.

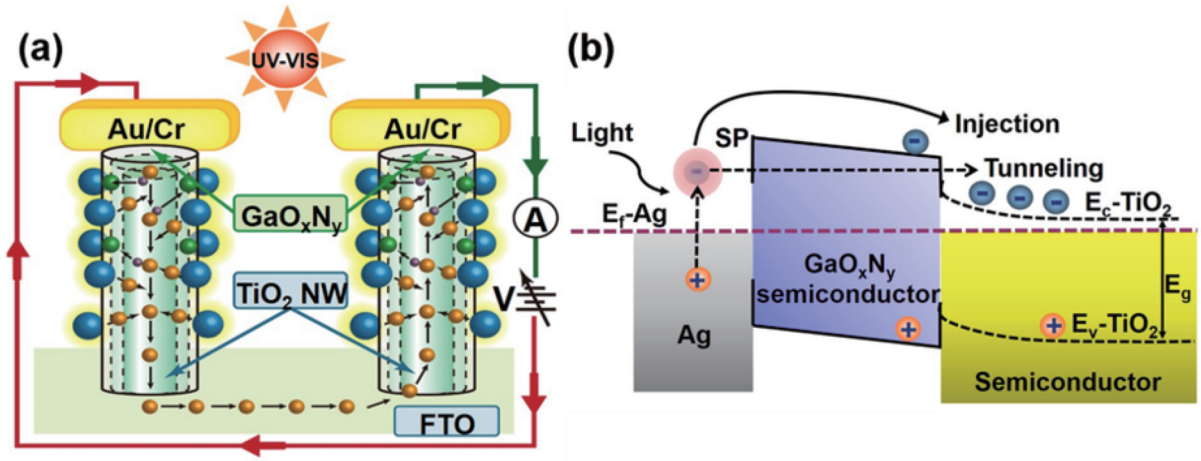

Fig. 6. (Color online) (a) Schematic band diagram of TiO_2@GaO_xN_y-Ag demonstrating the behaviour of charge transport. (b) The energy band diagram illustrating the transport properties of the TiO_2@GaO_xN_y-Ag heterojunction.

into hot electrons and holes, which further enhanced the flow of electrons. Accordingly, the generated holes of TiO_2@GaO_xN_y and UV-VIS photons recombined with few oxygens trapped electrons, which release energy and benefit for discharging the negatively charge oxygen ions. Therefore, the trapped electrons of TiO_2@GaO_xN_y-Ag are released, which also increase the density of electrons. The cumulatively generated charge carriers were drifted with the applied electric field along the [001] direction of TiO_2 NWs. Fig. 6(b) shows the band diagram of the heterojunction and charge separation in the photoelectric process. The improved photoelectric detection performance mainly originated from the MSM heterojunction and SPR effect of Ag. However, as light interacted with Ag, SPR was generated, which decayed into hot electrons and holes[45]. Hot electrons crossed the potential barrier of the heterojunction and reached the conduction band of TiO_2 through tunnelling and direct injection, which generated a photocurrent[46]. While, the valence and conduction

bands of GaO_xN_y were higher than that of TiO_2, thus forming the type-Ⅱ GaO_xN_y@TiO_2 heterojunction. When light interacted with the heterojunction, electrons moved from GaO_xN_y to TiO_2 in the conduction band and holes moved from TiO_2 to GaO_xN_y in the valence band, which effectively promoted the separation of photogenerated carriers and reduced the recombination rate. The unique GaO_xN_y@TiO_2 core-shell structure also provided an effective contact area and direct path for the photoelectric process and transmission of electrons and holes. These advantages can improve the efficiency and response time of photoelectric detection.

3. Conclusion

In summary, TiO_2@GaO_xN_y-Ag ternary heterojunction nanowire arrays were prepared using the hydrothermal, ALD, and photodecomposition methods. The MSM-type photodetector was developed using this ternary heterojunction. At 380 nm, the R and D of TiO_2@GaO_xN_y-Ag were 0.94 A/W and 4.79×10^9 Jones, respectively, and they increased to 2.86 A/W and 7.96×10^{10} Jones at 580 nm. The rise and fall times of the response were 0.19/0.23 and 0.50/0.57 s, respectively. In particular, the R of our device at 580 nm is one to four orders of magnitude higher than the same type of photodetectors based on TiO_2, Ga_2O_3, and other heterojunctions. Evidenced through FDTD simulations and photoelectric measurements, its excellent optoelectronic characteristics of the photodetector are mainly attributed to the synergistic effect of the type-Ⅱ band structure of the MSM heterojunction and the plasmon resonance effect of Ag, which not only effectively promoted the separation of photogenerated carriers but also reduced the recombination rate. This study provides the insights into the design of composite heterojunction detectors and the construction of wide band, high-performance detectors in the future.

Acknowledgements

This work was supported by National Natural Science Foundation of China (Nos. 62027818, 61874034, and 51861135105), and Natural Science Foundation of Shanghai (No. 18ZR1405000), Shanghai Science and Technology Innovation Program (No. 19520711500).

Appendix A. Supplementary materials

Supplementary materials to this article can be found online at https://doi.org/1674-4926/44/7/072806.

References

[1] Rathkanthiwar S, Kalra A, Solanke S V, et al. Gain mechanism and carrier transport in high responsivity AlGaN-based solar blind metal semiconductor metal photodetectors. J Appl Phys, 2017, 121, 164502

[2] Hwang J D, Yang C C, Chu C M. MgZnO/ZnO two-dimensional electron gas photodetectors fabricated by radio frequency sputtering. ACS Appl Mater Interfaces, 2017, 9, 23904

[3] Guo D Y, Chen K, Wang S L, et al. Self-powered solar-blind photodetectors based on α/β phase junction of Ga_2O_3. Phys Rev Appl, 2020, 13, 024051

[4] Wu C, Wu F M, Hu H Z, et al. Review of self-powered solar-blind photodetectors based on Ga_2O_3. Mater Today Phys, 2022, 28, 100883

[5] He C R, Guo D Y, Chen K, et al. α-Ga_2O_3 nanorod array–Cu_2O microsphere *p*–*n* junctions for self-powered spectrum-distinguishable photodetectors. ACS Appl Nano Mater, 2019, 2, 4095

[6] Dubourg G, Radović M. Multifunctional screen-printed TiO_2 nanoparticles tuned by laser irradiation for a flexible and scalable UV detector and room-temperature ethanol sensor. ACS Appl Mater Interfaces, 2019, 11, 6257

[7] Khan I, Qurashi A, Berdiyorov G, et al. Single-step strategy for the fabrication of GaON/ZnO nanoarchitectured photoanode their experimental and computational photoelectrochemical water splitting. Nano Energy, 2018, 44, 23

[8] Qin Y, Li L H, Zhao X L, et al. Metal–semiconductor–metal ε-Ga_2O_3 solar-blind photodetectors with a record-high responsivity rejection ratio and their gain mechanism. ACS Photonics, 2020, 7, 812

[9] Zheng L X, Hu K, Teng F, et al. Novel UV–visible photodetector in photovoltaic mode with fast response and ultrahigh photosensitivity employing Se/TiO_2 nanotubes heterojunction. Small, 2017, 13, 1602448

[10] Wang J L, Li S P, Wang T T, et al. Solution-processed Sb_2Se_3 on TiO_2 thin films toward oxidation- and moisture-resistant, self-powered photodetectors. ACS Appl Mater Interfaces, 2020, 12, 38341

[11] Jeong K, Deshmukh P R, Park J, et al. ZnO-TiO_2 core–shell nanowires: A sustainable photoanode for enhanced photoelectrochemical water splitting. ACS Sustainable Chem Eng, 2018, 6, 6518

[12] Feng W J, Lin L Y, Li H J, et al. Hydrogenated TiO_2/ZnO heterojunction nanorod arrays with enhanced performance for photoelectrochemical water splitting. Int J Hydrog Energy, 2017, 42, 3938

[13] Kim H S, Jeon S H, Park J S, et al. Anion control as a strategy to achieve high-mobility and high-stability oxide thin-film transistors. Sci Rep, 2013, 3, 1459

[14] Koo A, Budde F, Ruck B J, et al. Photoconductivity in nanocrystalline GaN and amorphous GaON. J Appl Phys, 2006, 99, 034312

[15] Hu C C, Lee Y L, Teng H. Influence of indium doping on the activity of gallium oxynitride for water splitting under visible light irradiation. J Phys Chem C, 2011, 115, 2805

[16] Raza M H, Kaur N, Comini E, et al. Toward optimized radial modulation of the space-charge region in one-dimensional SnO_2-NiO core-shell nanowires for hydrogen sensing. ACS Appl Mater Interfaces, 2020, 12, 4594

[17] Ismail F M, O'Neil D, Youssef T, et al. Ultrafast laser dynamics of metal organic frameworks/TiO_2 nano-arrays hybrid composites for energy conversion applications. J Energy Chem, 2019, 29, 88

[18] Yang D M, Ren Y X, Du F Q, et al. Enhanced response speed of TiO_2 nanoarrays based all solid-state ultraviolet photodetector via SiO_2 dielectric layer. J Alloys Compd, 2021, 867, 159053

[19] Brolo A G. Plasmonics for future biosensors. Nat Photonics, 2012, 6, 709

[20] Kale M, Christopher P. Plasmons at the interface. Science, 2015, 349, 587

[21] Mubeen S, Lee J, Lee W, et al. On the plasmonic photovoltaic. ACS Nano, 2014, 8, 6066

[22] García de Arquer F P, Mihi A, Kufer D, et al. Photoelectric energy conversion of plasmon-generated hot carriers in metal-insulator-semiconductor structures. ACS Nano, 2013, 7, 3581

[23] Bechambi O, Chalbi M, Najjar W, et al. Photocatalytic activity of ZnO doped with Ag on the degradation of endocrine disrupting under UV irradiation and the investigation of its antibacterial activity. Appl Surf Sci, 2015, 347, 414

[24] Huang H L, Hou X L, Xiao J R, et al. Effect of annealing atmosphere on the performance of TiO_2 nanorod arrays in photoelectrochemical water splitting. Catal Today, 2019, 330, 189

[25] Abd-Lefdil M, Diaz R, Bihri H, et al. Preparation and characterization of sprayed FTO thin films. Eur Phys J Appl Phys, 2007, 38, 217

[26] Jung Y, Ahn J, Baik K H, et al. Chemical etch characteristics of N-face and Ga-face GaN by phosphoric acid and potassium hydroxide solutions. J Electrochem Soc, 2011, 159, H117
[27] Asakura Y, Inaguma Y, Ueda K, et al. Synthesis of gallium oxynitride nanoparticles through hydrothermal reaction in the presence of acetylene black and their photocatalytic NO_x decomposition. Nanoscale, 2018, 10, 1837
[28] Cailleaux X, del Carmen Marco de Lucas M, Merdrignac-Conanec O, et al. Structural study of gallium oxynitrides prepared by ammonolysis of different oxide precursors. J Phys D: Appl Phys, 2009, 42, 045408
[29] Maeda K, Teramura K, Takata T, et al. Overall water splitting on $(Ga_{1-x}Zn_x)(N_{1-x}O_x)$ solid solution photocatalyst: relationship between physical properties and photocatalytic activity. J Phys Chem B, 2005, 109, 20504
[30] Yang Z W, Wang B, Cui H, et al. Synthesis of crystal-controlled TiO_2 nanorods by a hydrothermal method: Rutile and brookite as highly active photocatalysts. J Phys Chem C, 2015, 119, 16905
[31] Hattori A N, Endo K, Hattori K, et al. Surface treatments toward obtaining clean GaN(0001) from commercial hydride vapor phase epitaxy and metal-organic chemical vapor deposition substrates in ultrahigh vacuum. Appl Surf Sci, 2010, 256, 4745
[32] Zhang L, Wang S Z, Shao Y L, et al. One-step fabrication of porous GaN crystal membrane and its application in energy storage. Sci Rep, 2017, 7, 44063
[33] Maeda K, Domen K. Oxynitride materials for solar water splitting. MRS Bull, 2011, 36, 25
[34] Yu D H, Yu X D, Wang C H, et al. Synthesis of natural cellulose-templated TiO_2/Ag nanosponge composites and photocatalytic properties. ACS Appl Mater Interfaces, 2012, 4, 2781
[35] Shi H X, Chen J Y, Li G Y, et al. Synthesis and characterization of novel plasmonic Ag/AgX-CNTs (X = Cl, Br, I) nanocomposite photocatalysts and synergetic degradation of organic pollutant under visible light. ACS Appl Mater Interfaces, 2013, 5, 6959
[36] Li L, Zhang X L, Zhang W Z, et al. Microwave-assisted synthesis of nanocomposite Ag/ZnO–TiO_2 and photocatalytic degradation Rhodamine B with different modes. Colloids Surf A Physicochem Eng Aspects, 2014, 457, 134
[37] Karbalaei Akbari M, Hai Z Y, Wei Z H, et al. ALD-developed plasmonic two-dimensional Au-WO_3-TiO_2 heterojunction architectonics for design of photovoltaic devices. ACS Appl Mater Interfaces, 2018, 10, 10304
[38] Yang C P, Chang S P, Chang S J, et al. Bandgap engineered ultraviolet photodetectors with gallium-zinc-oxide via Co-sputtering method. ECS J Solid State Sci Technol, 2018, 7, Q3083
[39] Ouyang W X, Teng F, Fang X S. High performance BiOCl nanosheets/TiO_2 nanotube arrays heterojunction UV photodetector: The influences of self-induced inner electric fields in the BiOCl nanosheets. Adv Funct Mater, 2018, 28, 1707178
[40] Xu X J, Chen J X, Cai S, et al. A real-time wearable UV-radiation monitor based on a high-performance p-CuZnS/n-TiO_2 photodetector. Adv Mater, 2018, 30, 1803165
[41] Zheng L X, Deng X L, Wang Y Z, et al. Self-powered flexible TiO_2 fibrous photodetectors: Heterojunction with P3HT and boosted responsivity and selectivity by Au nanoparticles. Adv Funct Mater, 2020, 30, 2001604
[42] Zhou M, Wu B Z, Zhang X T, et al. Preparation and UV photoelectric properties of aligned ZnO-TiO_2 and TiO_2-ZnO core-shell structured heterojunction nanotubes. ACS Appl Mater Interfaces, 2020, 12, 38490
[43] Zhang Y, Xu W X, Xu X J, et al. Low-cost writing method for self-powered paper-based UV photodetectors utilizing Te/TiO_2 and Te/ZnO heterojunctions. Nanoscale Horiz, 2019, 4, 452
[44] Joshna P, Hazra A, Chappanda K N, et al. Fast response of UV photodetector based on Ag nanoparticles embedded uniform TiO_2 nanotubes array. Semicond Sci Technol, 2020, 35, 015001
[45] Zhou X, Zhang Q, Gan L, et al. High-performance solar-blind deep ultraviolet photodetector based on individual single-crystalline Zn_2GeO_4 nanowire. Adv Funct Mater, 2016, 26, 704
[46] Zhang Y F, Chen X H, Xu Y, et al. Anion engineering enhanced response speed and tunable spectral responsivity in gallium-oxynitrides-based ultraviolet photodetectors. ACS Appl Electron Mater, 2020, 2, 808
[47] Ma H P, Li X X, Yang J H, et al. Composition and properties control growth of high-quality GaO_xN_y film by one-step plasma-enhanced atomic layer deposition. Chem Mater, 2019, 31, 7405
[48] Dubey A, Mishra R, Hsieh Y H, et al. Aluminum plasmonics enriched ultraviolet GaN photodetector with ultrahigh responsivity, detectivity, and broad bandwidth. Adv Sci, 2020, 7, 2002274

Jiajia Tao received the Ph.D. degree in School of Microelectronics, Fudan University, Shanghai, China. He is currently a senior engineer in the 50th Research Institute of China Electronics Technology Group Corporation, Shanghai, China. His main research interests include ALD Ga_2O_3-based photodetectors, low-dimensional material optoelectronic devices, and functional module design for Si-based chips.

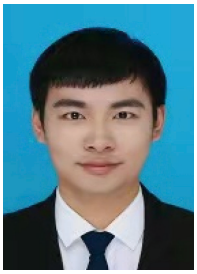

Guang Zeng is a Ph.D. candidate in School of Microelectronics, Fudan University, Shanghai, China. His main research interests include solar-blind photodetectors based on β-Ga_2O_3, waveguide-integrated low-dimensional material photodetectors, and low-dimensional material optoelectronic devices.

Hongliang Lu is a professor and doctoral supervisor in the School of Microelectronics, Fudan University. His main research direction is new semiconductor materials and devices for the next generation of Integrated Circuit (IC) technology. In the meantime, he has published more than 200 papers in international academic journals and 20 domestic patents.